Article

Photoactivated Nanohybrid for Dual-Nuclei MR/US/PA Multimodal-Guided Photothermal Therapy

Shizhen Chen,[†] Maosong Qiu,[†] Ruifang Wang, Lei Zhang, Conggang Li, Chaohui Ye, and Xin Zhou*

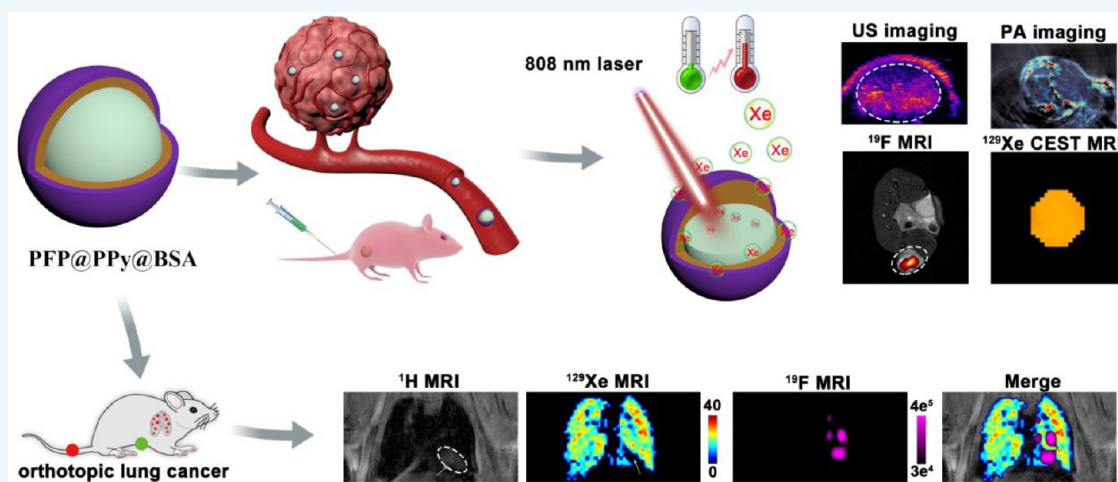Cite This: *Bioconjugate Chem.* 2022, 33, 1729−1740

Read Online

ACCESS | Metrics & More | Article Recommendations | Supporting Information

ABSTRACT: Nanohybrids have gained immense popularity for the diagnosis and chemotherapy of lung cancer for their excellent biocompatibility, biodegradability, and targeting ability. However, most of them suffer from limited imaging information, low tumor-to-background ratios, and multidrug resistance, limiting their potential clinical application. Herein, we engineered a photoresponsive nanohybrid by assembling polypyrrole@bovine serum albumin (PPy@BSA) encapsulating perfluoropentane (PFP)/^{129}Xe for selective magnetic resonance (MR)/ultrasonic (US)/photoacoustic (PA) trimodal imaging and photothermal therapy of lung cancer, overcoming these drawbacks of single imaging modality and chemotherapy. The nanohybrid exhibited superior US, PA, and MR multimodal imaging performance for lung cancer detection. The high sensitivity of the nanohybrid to near-infrared light (NIR) resulted in a rapid increase in temperature in a low-intensity laser state, which initiated the phase transition of liquid PFP into the gas. The ultrasound signal inside the tumor, which is almost zero initially, is dramatically increased. Beyond this, it led to the complete depression of ^{19}F/^{129}Xe Hyper-CEST (chemical exchange saturation transfer) MRI during laser irradiation, which can precisely locate lung cancer. *In vitro* and *in vivo* results of the nanohybrid exhibited a successful therapeutic effect on lung cancer. Under the guidance of imaging results, a sound effect of photothermal therapy (PTT) for lung cancer was achieved. We expect this nanohybrid and photosensitive behavior will be helpful as fundamental tools to decipher lung cancer in an earlier stage through trimodality imaging methods.

■ INTRODUCTION

As the most common cancer, lung cancer brings grave harm to human beings. Unfortunately, most patients with lung cancer are diagnosed as advanced and have only a 5-year survival.[1] Compared with chest X-ray, X-ray computed tomography (CT) has turned out to be an effective channel to detect early lung cancer and reduce mortality.[2] However, CT screening suffers from ionizing radiation, and the accurate tumor diagnosis is still unsatisfactory. Activatable theranostics provide advanced solutions for tumor diagnosis by enhancing contrast in various imaging technologies and tailored therapy.[3−10] With more diagnostic information, multimodal imaging can diagnose tumors more accurately than single imaging.[11−17] So far,

positron emission computed tomography (PET)/CT and PET/magnetic resonance imaging (MRI) have been extensively used in the biomedical field,[18] which facilitate the fabrication of multiple responsive and multimodal contrast agents for tumor diagnosis. In addition, there is an urgent need
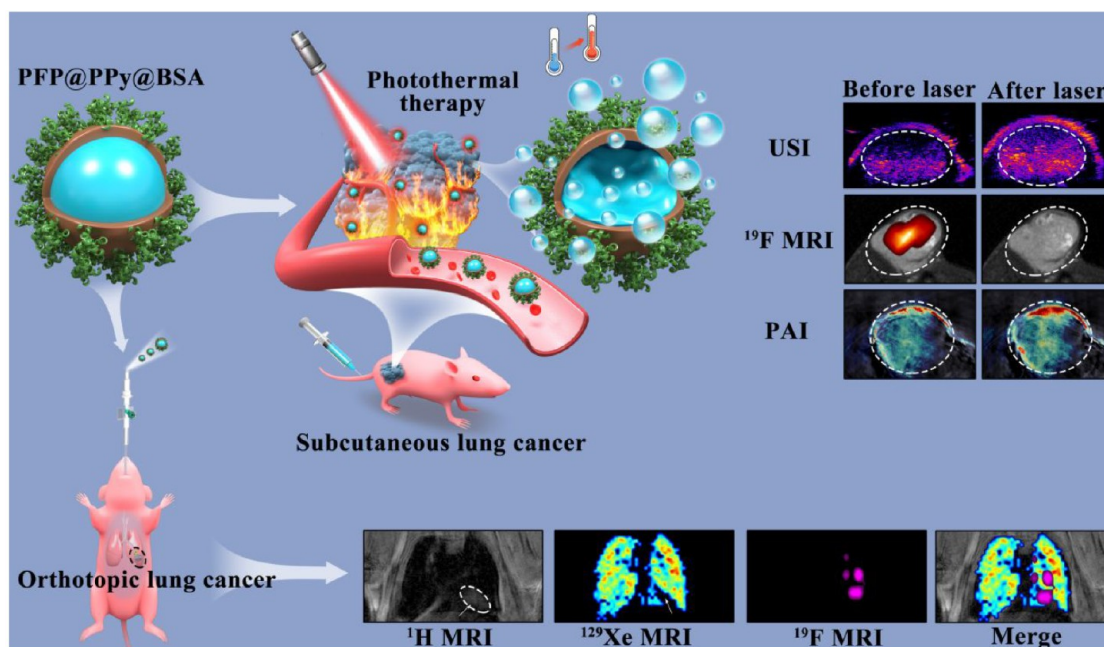
Scheme 1. Schematic Illustration of PFP@PPy@BSA for ^{19}F/^{129}Xe Dual-Nuclei MR/PA/US Multimodal Imaging and Photothermal Therapy[a]

[a]The liquid PFP inside the nanohybrid can be changed to bubbles when the temperature was increased in the tumor region via the photothermal effect of PPy under laser irradiation. With the liquid−gas transition of PFP, the ^{19}F and ^{129}Xe Hyper-CEST MRI signals would be switched from "on" to "off". Integrating the enhancement of the US signal and the "on−off" transition of ^{129}Xe/^{19}F MRI signals upon laser irradiation, the nanohybrid held great promise for accurate localization of lung cancer.

to combine various excellent imaging methods such as MRI, ultrasonic imaging (USI), and photoacoustic imaging (PAI) to develop multimodal imaging methods for the early diagnosis of malignant tumors.[19−25] ^{1}H MRI with excellent spatial resolution and unlimited penetration depth can aid in detecting deep-seated cancers but is hampered by high background signals from normal tissues and low sensitivity.[26−30] As a vibrant complementary method, ^{19}F MRI without background signal and hyperpolarized ^{129}Xe MRI with ultrahigh sensitivity have received intense attention.[31−38] Specifically, hyperpolarized ^{129}Xe MRI has been applied to evaluate pulmonary function in COVID-19 patients.[39]

For its high spatial selectivity and noninvasiveness, near-infrared photothermal therapy (NIR-PTT) has been widely studied for precise cancer therapy.[40−42] In detail, PTT uses photothermal reagents to transform light into local heat energy, thereby destroying tumors. NIR-PTT has been proved to be an available technique for the treatment of malignant tumors in clinical practice by heat-induced coagulation necrosis of tumor tissues.[43] To date, various types of photothermal reagents have been constructed, including polypyrrole (PPy),[44] polydopamine,[45] Au nanorods,[46] Prussian blue,[47] and CuS.[48] PPy has been widely used in tumor diagnosis and PTT because of its excellent biocompatibility and photothermal properties. Shi et al. developed a novel PPy nanomaterial with excellent photothermal conversion capability and confirmed its extraordinary therapeutic effect on tumors.[49] Zhou et al. synthesized a PPy nanohybrid, where they authenticated the safe use of PPy-based MRI-guided NIR-PTT in 4T1 tumors.[50] On the other hand, most nanohybrids have "always-on" signals, resulting in low tumor-to-background ratios (TBRs).[51] Recently, nanohybrid enhancing image signals via photoresponse have attracted much attention. Although

several photoresponsive probes have been widely used for diagnosis and PTT of malignant tumors, they can only enhance US signals. So far, nanohybrids with the simultaneous photoresponsive transformation of US and MRI signals have not been reported.

Herein, a perfluoropentane (PFP)-loaded nanohybrid with PPy and bovine serum albumin (BSA) shells (PFP@PPy@BSA) was fabricated for multimodal imaging and PTT of lung cancer (Scheme 1). The modification of PPy endowed the nanohybrid with a superior photothermal property and photoacoustic effect. And BSA plays an important role in improving the water dispersibility and biocompatibility.[52−54] The as-prepared nanohybrid could disperse nicely in a buffer environment and passively target tumors through the enhanced permeation and retention (EPR) effect, allowing for US/^{19}F MR/^{129}Xe Hyper-CEST (chemical exchange saturation transfer) MR/PA multimodal imaging and PTT for lung cancer. Most notably, the liquid PFP can be transformed into microbubbles upon NIR laser irradiation to enhance the USI signal of tumors. With the liquid−gas transition of PFP, the ^{19}F and ^{129}Xe Hyper-CEST MRI signals would be switched from "on" to "off". Integrating the enhancement of the US signal and the "on−off" transition of ^{129}Xe/^{19}F MRI signals upon laser irradiation, the nanohybrid held great promise for accurate localization of lung cancer. Therefore, PFP@PPy@BSA is a versatile nanoplatform, which can realize accurate and efficient PTT of lung cancer under the guidance of photoresponsive multimodal imaging.

■ RESULTS AND DISCUSSION

Fabrication and Characterization of the Nanohybrid. The PFC@PPy@BSA nanohybrids were synthesized via three steps. First, the perfluorocarbon (PFC) microemulsions were
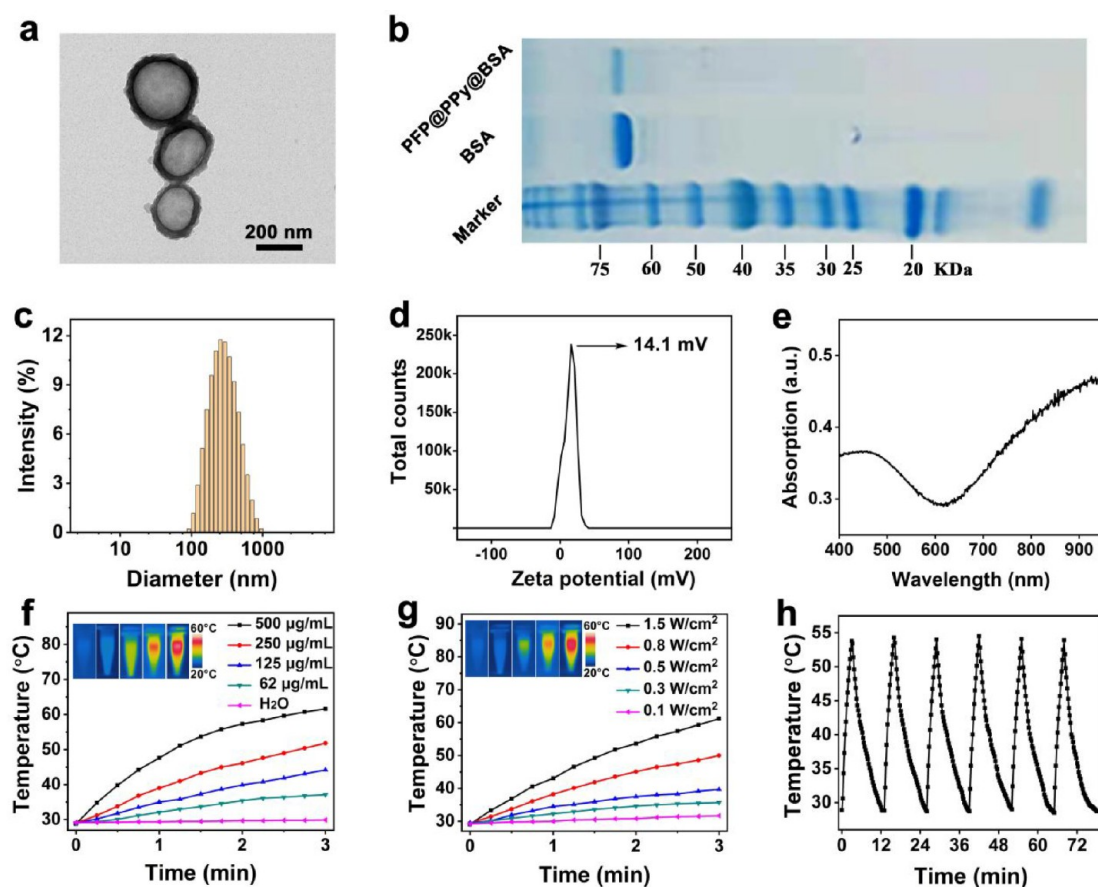
Figure 1. Characterization of PFP@PPy@BSA. (a) TEM image of PFP@PPy@BSA. (b) SDS-PAGE protein analysis of BSA and PFP@PPy@BSA. (c) Hydrodynamic size of PFP@PPy@BSA. (d) Zeta potential of PFP@PPy@BSA. (e) UV−vis−NIR absorbance spectra of PFP@PPy@BSA. (f) Temperature rise profiles of PFP@PPy@BSA with various concentrations under laser irradiation (1.0 W/cm^2). (g) Temperature rise profiles of PFP@PPy@BSA under laser irradiation with diversified power densities (PFP@PPy@BSA: 250 μg/mL). (h) Photothermal stability of PFP@PPy@BSA within six cycles of NIR laser irradiation.

generated by pulsed sonication for 40 min. Next, ferric ions (Fe^{3+}) were utilized to oxidize the pyrrole monomer, yielding the PPy layer on the PFCs microemulsion. Finally, the BSA was added to the mixture and further stirred for 4 h, and the monodisperse PFC@PPy@BSA nanohybrid was obtained. To verify the feasibility and generality of this facile functionalization method, different perfluorocarbons (PFCs) including PFP, pperfluorohexane (PFH), perfluorooctylbromide (PFOB), perfluoro-15-crown-5 (PFCE), and perfluorononane (PFN) (Figure S1) were used to fabricate the PFC@PPy@BSA. The results of ^{19}F NMR characterizations demonstrated that all the PFC@PPy@BSA NPs were successfully loaded with PFCs and that the PFCs' (PFP, PFH, PFOB, PFCE, and PFN) loading efficiencies of PFC@PPy@BSA were calculated to be 53.0%, 52.0%, 47.4%, 63.6%, and 62.3%, respectively (Figures S3 and S4). Because the boiling point of PFP is most suitable for the photothermally excited phase transition *in vivo*, PFP@PPy@BSA was selected for further study. The spherical PFP@PPy@BSA nanohybrid was about 270 nm in diameter, and the BSA shell thickness was about 30 nm, examined by TEM. The similar protein profiles between nanohybrid and BSA characterized by the SDS-PAGE experiment proved that the BSA was successfully decorated onto the nanohybrid (Figure 1b). The hydrodynamic diameter of the nanohybrid was 329 ± 90 nm, and the zeta potential was 14.1 ± 2.4 mV (Figure 1c and d).

The PFP@PPy@BSA aqueous solution exhibited absorbance in the NIR region (Figure 1e), indicating the presence of PPy. Upon NIR laser irradiation at 808 nm, with the increase of nanohybrid concentration, the temperature rise range increased from 8 to 32.8 °C (Figure 1f). Afterward, the 250 μg/mL of nanohybrid was irradiated with various laser power densities, and the highest temperature elevation was up to 50 °C (Figure 1g). Meanwhile, by doing six cycles of lasing on−off processes, the temperature values were almost the same for the on and off states, demonstrating good photothermal stability of PFP@PPy@BSA (Figure 1h). In light of the change in the temperature, the photothermal conversion efficiency (PTCE) of the nanohybrid was calculated as 59.2% using the previously reported method.[55] The outstanding PTCE could be utilized for the light-responsive liquid−gas transition of PFP and the PTT of malignant tumors.

***In Vitro* Trimodal Imaging Properties of the Nanohybrid and Its Light-Responsive Behavior.** The PFP@PPy@BSA aqueous solution displayed three ^{19}F NMR peaks at −84.2, −126.1, and −129.0 ppm, aligning well with the signals of PFP (Figures 2a and S3). Since the relaxation time of PFP can affect the intensity of the ^{19}F signal, the transverse relaxation times (T_2) of the PFP@PPy@BSA nanohybrid were examined at three different temperatures. The results displayed that the transverse relaxation times of the PFP@PPy@BSA (-CF$_3$) at all three temperatures exceeded 500 ms, which was
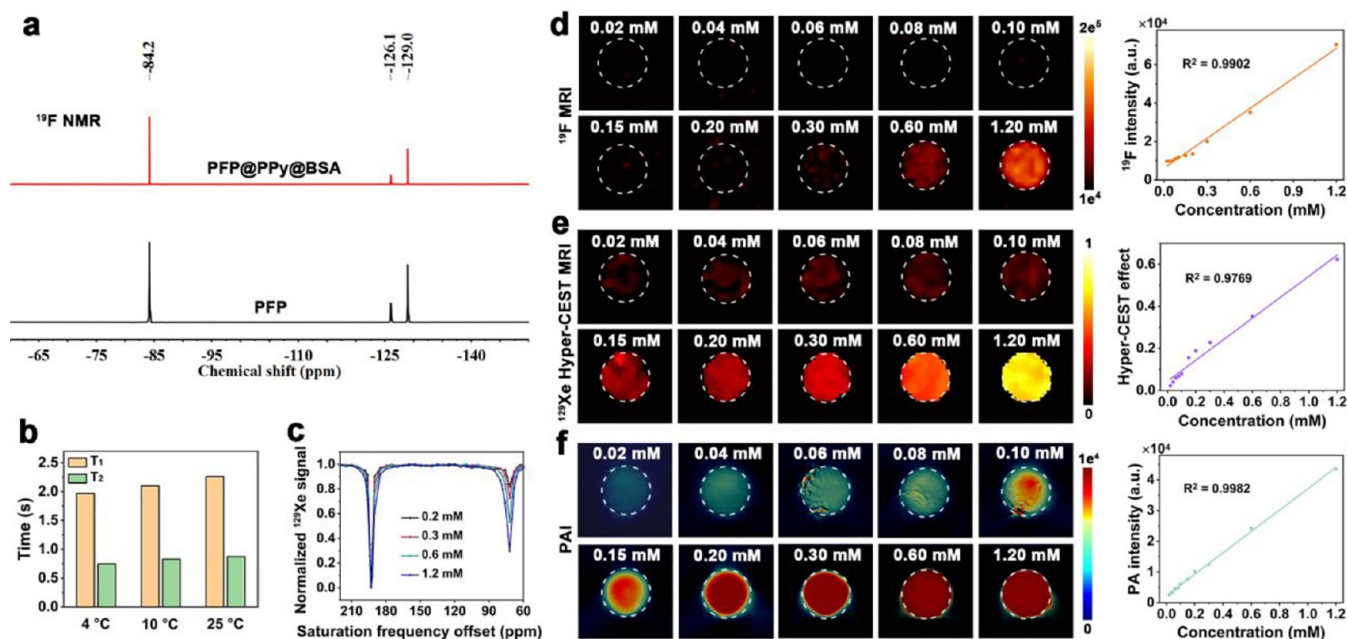
Figure 2. *In vitro* multimodal imaging of PFP@PPy@BSA. (a) ^{19}F NMR spectra of PFP@PPy@BSA and PFP. (b) T_1 and T_2 values of PFP@PPy@BSA (-CF$_3$) at different temperatures. (c) ^{129}Xe Hyper-CEST spectra at different concentrations (C$_{PFP}$ = 0.2, 0.3, 0.6, 1.2 mM) of PFP@PPy@BSA. (d−f) *In vitro* ^{19}F MR, ^{129}Xe Hyper-CEST MR, and PA trimodal imaging (left) of PFP@PPy@BSA aqueous solution at different concentrations (C$_{PFP}$ = 0.02, 0.04, 0.06, 0.08, 0.12, 0.20, 0.30, 0.60, 1.20 mM) and the relationship (right) between signal intensity and PFP@PPy@BSA concentration.

sufficient to acquire an outstanding ^{19}F MRI (Figures 2b and S5). Beyond that, the relaxation times (T_1 and T_2) of PFP@PPy@BSA (-CF$_3$) were longer than those of other PFC@PPy@BSA nanohybrids (-CF$_3$ or -CF$_2$), which were more suitable for ^{19}F MRI. The most prominent peak of the ^{19}F NMR spectrum was at −84.2 ppm, which was used for ^{19}F MRI experiments. The signal intensity of the ^{19}F MRI showed a linear relationship with the PFP concentration in the nanoparticle, with the detection limit of 0.6 mM (C$_{PFP}$) (Figure 2d).

Due to the high Ostwald solubility of ^{129}Xe in liquid PFP, the ^{129}Xe Hyper-CEST of PFP@PPy@BSA at different concentrations was studied. The chemical shift of the captured ^{129}Xe atoms in PFP was 72 ppm, far from the state in the water solution (192.6 ppm) (Figure 2c). Nevertheless, this is beneficial for the ^{129}Xe Hyper-CEST signal differentiation. Besides, with the PFP concentration increased, the ^{129}Xe Hyper-CEST signal intensity of PFP@PPy@BSA gradually enhanced. The moderate exchange rate is significant for efficient ^{129}Xe Hyper-CEST detection because the fast exchange rate will broaden the ^{129}Xe Hyper-CEST peak. The exchange rates of ^{129}Xe atoms in PFP@PPy@BSA, PFH@PPy@BSA, PFOB@PPy@BSA, PFCE@PPy@BSA, and PFN@PPy@BSA were 365, 610, 238, 1682, and 1676 s^{-1}, respectively (Figure S7), among which the exchange rates of PFP@PPy@BSA and PFOB@PPy@BSA are more appropriate. Considering the relaxation times of PFC, the exchange rate of ^{129}Xe, and the application *in vivo*, PFP@PPy@BSA was finally selected for MR/US/PA trimodal imaging. Phantom experiments showed that the ^{129}Xe Hyper-CEST MRI signal intensity was linearly correlated with PFP@PPy@BSA concentration (Figure 2e). Compared with ^{19}F MRI, the ^{129}Xe MRI signal can be detected at a lower concentration (as low as 0.02 mM). These properties indicated that the PFP@

PPy@BSA could be a potential ^{129}Xe biosensor for biomedical imaging experiments. In addition, owing to the strong NIR absorbance, PFP@PPy@BSA can be used as an effective probe for PAI. As expected, the PA signal intensities of PFP@PPy@BSA aqueous solutions were also linearly proportional to their PFP concentrations (Figure 2f). The imaging results exhibited that the PFP@PPy@BSA nanohybrid could be a promising candidate for trimodal imaging.

PFP is biocompatible and widely exploited as the ultrasound contrast agent.[56] The phase transition of PFP can induce microbubbles, providing enhanced US contrast. Due to the high pressure in the body, the boiling point of PFP rises from 29 °C to 40−50 °C.[57] Consequently, the phase transition of the PFP cargo will be triggered when the temperature is raised above its boiling point upon laser irradiation. The optical microscopy image displayed obvious microbubbles in PFP@PPy@BSA aqueous solution after laser irradiation, demonstrating that the laser induced a phase transition in PFP which can be utilized in ultrasound imaging (Figure S8). Subsequently, the US imaging property of PFP@PPy@BSA was investigated by using the B-mode under 808 nm laser irradiation or not. A prominent US signal of the PFP@PPy@BSA nanohybrid was observed, and the signal intensity of the nanohybrid was significantly enhanced after laser exposure (Figure S9a).

In contrast, a weak US signal and no apparent change with laser exposure were observed for pure buffer solution. Considering that the ^{19}F/^{129}Xe Hyper-CEST MRI signals came from PFP, the phase transition of PFP may lead to the disappearance of the MRI signals. To prove this conjecture, NMR and MRI of the PFP@PPy@BSA aqueous solution were performed before and after laser irradiation. As expected, the apparent ^{19}F NMR and ^{129}Xe Hyper-CEST signals of the nanohybrid solution were obtained before the laser exposure but disappeared unanimously after exposure to laser irradiation
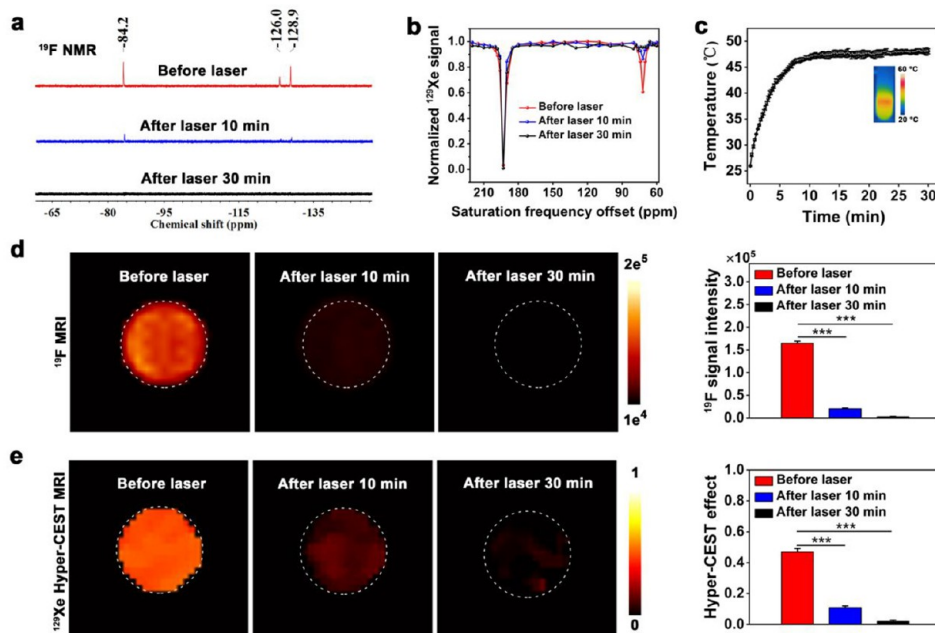
Figure 3. *In vitro* cellular photoresponsive ^{19}F/^{129}Xe Hyper-CEST MRI of PFP@PPy@BSA. (a) ^{19}F NMR and (b) ^{129}Xe Hyper-CEST spectra of A549 cells treated with PFP@PPy@BSA before and after laser irradiation (1.0 W/cm^2) for 10 and 30 min. (c) Temperature changes of A549 cells treated with PFP@PPy@BSA upon laser irradiation (1.0 W/cm^2) for 30 min. (d) ^{19}F MRI and the corresponding signal intensity of A549 cells treated with PFP@PPy@BSA before and after laser irradiation (1.0 W/cm^2) for 10 and 30 min. (e) ^{129}Xe Hyper-CEST MRI and the corresponding Hyper-CEST effect of A549 cells treated with PFP@PPy@BSA before and after laser irradiation (1.0 W/cm^2) for 10 and 30 min. ***$P < 0.001$, $n = 3$, data represent mean $\pm$ SD.
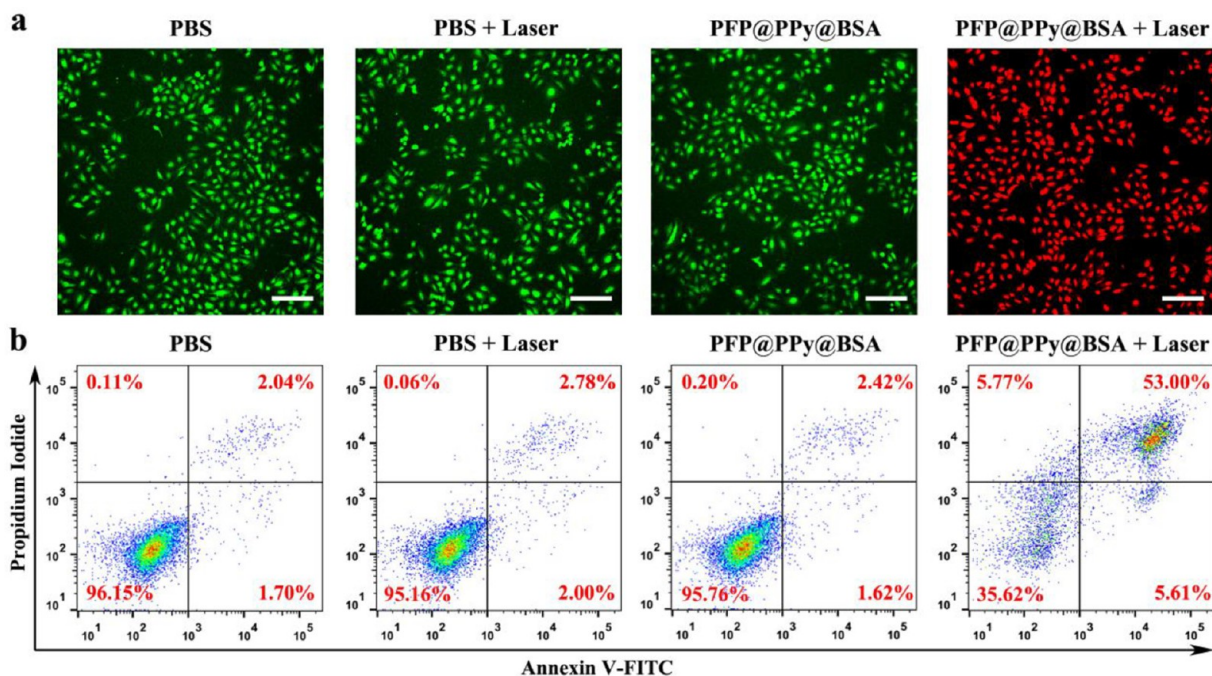

Figure 4. *In vitro* PTT of PFP@PPy@BSA. (a) CLSM images of calcein-AM/PI-based A549 cell staining (Scale bar: 200 μm). (b) Cell apoptosis of A549 cells with various treatments.

(Figure S9b–e). Similar results were observed from the imaging experiment.

Cellular Light-Responsive MRI and Photothermal Cytotoxicity. Before applying PFP@PPy@BSA to image living cells, the cytotoxicities against A549 lung cancer cells and MRC-5 embryonic lung fibroblasts were determined by standard MTT assay and CCK8 assay. The results indicated

that PFP@PPy@BSA showed almost zero effect on cell viability against both cells, suggesting PFP@PPy@BSA had good cell biocompatibility (Figure S10). Afterward, A549 cells were coincubated with the PFP@PPy@BSA nanohybrid for 4, 8, 12, and 16 h to evaluate the cellular uptake behavior. The ^{19}F NMR experiments showed that cells were labeled by the nanohybrid, which could be mediated by phagocytosis (Figure
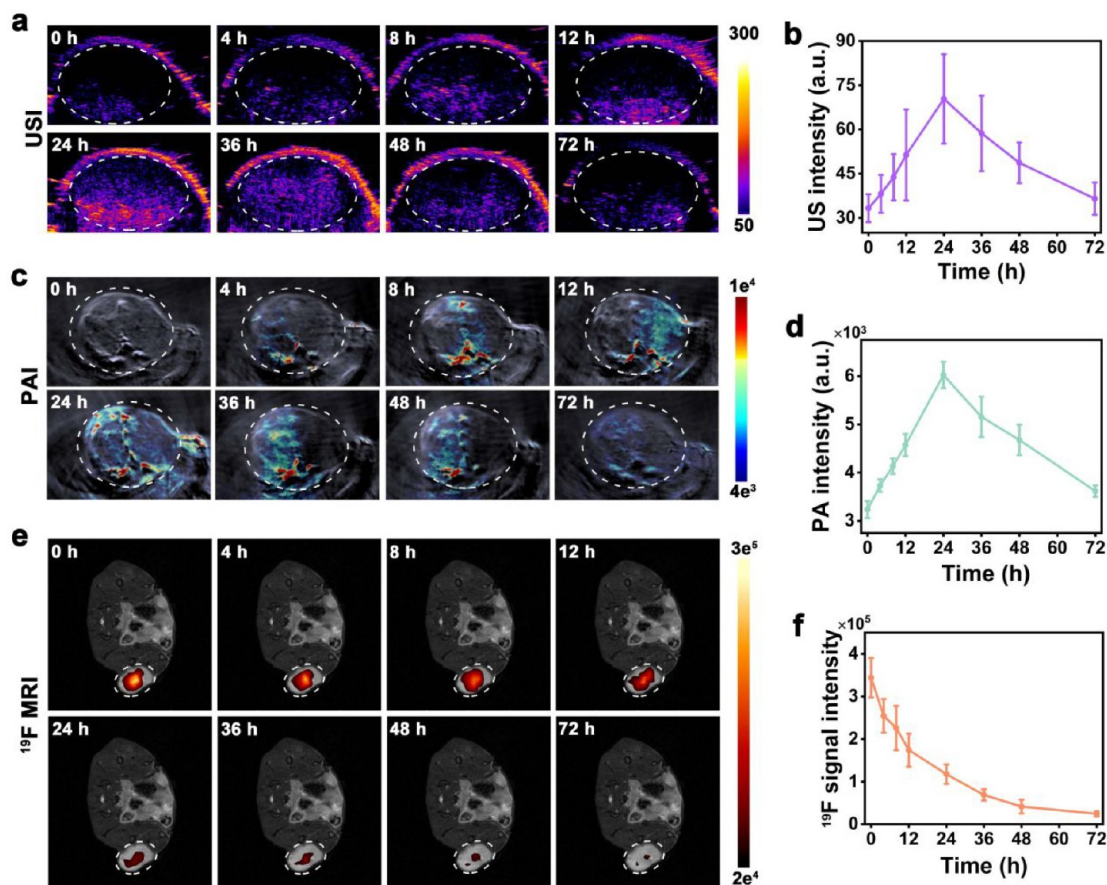
Figure 5. *In vivo* trimodal US/PA/^{19}F MR imaging. (a) US images of subcutaneous A549-tumor-bearing mice after *i.v.* injection of PFP@PPy@ BSA (C$_{PFP}$ = 18 mM, 200 μL) and (b) the corresponding quantification of tumor US intensity. (c) PA images of subcutaneous A549 tumors after *i.v.* injection of PFP@PPy@BSA (C$_{PFP}$ = 18 mM, 200 μL) and (d) the corresponding quantification of tumor PA intensity. (e) ^{19}F MRI of subcutaneous A549 tumors after intratumoral injection of PFP@PPy@BSA (C$_{PFP}$ = 30 mM, 50 μL) and (f) the corresponding quantification of tumor ^{19}F MRI signal intensity.

S11). The uptake of the PFP@PPy@BSA nanohybrid by A549 cells was a time-dependent process, and the accumulation reached the maximum value at 12 h. As emerged from these data, the PFP@PPy@BSA nanohybrid possessed great potential for photoresponsive ^{19}F/^{129}Xe Hyper-CEST MRI of living cells.

As expected, the ^{19}F NMR signals of A549 cells treated with nanohybrid were rapidly weakened after laser irradiation for 10 min and even disappeared after 30 min (Figure 3a). Similar to ^{19}F NMR, the cellular ^{129}Xe Hyper-CEST signals gradually vanished with the laser irradiation (Figure 3b and c). The average ^{19}F MRI signal intensity of A549 cells was reduced from 1.69×10^5 to 0.02×10^5 after laser irradiation for 30 min, and the cellular ^{129}Xe Hyper-CEST effect decreased from 49.2% to 1.0% (Figure 3d and e). As a control, the MRC-5 cells incubated with the PFP@PPy@BSA nanohybrid showed weaker ^{19}F/^{129}Xe Hyper-CEST NMR/MRI signals than A549 cells due to the relatively inferior uptake capacity (Figure S13). For these reasons, the PFP@PPy@BSA nanohybrid held excellent potential for *in vivo* photoresponsive trimodal imaging.

Next, the *in vitro* PTT performances of the PFP@PPy@BSA nanohybrid toward A549 and MRC-5 cells were investigated using the CCK8 assay. The results indicated that only the laser or the PFP@PPy@BSA nanohybrid had negligible cytotoxicity to the cell lines. By comparison, the cells treated with the

PFP@PPy@BSA nanohybrid that received laser irradiation showed apparent cytotoxicity, with over 80% of A549 cells and 35% of MRC-5 cells being killed (Figure S14a). The calcein-AM/PI two-stained assay was also tested to intuitively assess the anticancer effect of PTT (Figure 4a). Similarly, the PFP@PPy@BSA treated A549 cells within the laser irradiation area were severely damaged, indicated by significant red fluorescence, resulting in a clear border between the live and dead cells around the light spot (Figure S14b). By contrast, the A549 cells treated with laser or PFP@PPy@BSA alone exhibited a high survival rate. Flow cytometry of Annexin V-FITC/PI staining in A549 cells was carried out to further quantity the *in vitro* PTT efficiency of PFP@PPy@BSA (Figure 4b). Following a similar line, PBS alone, PBS plus laser, and PFP@PPy@BSA alone did not show apparent cell death (<5%). The A549 cells treated with PFP@PPy@BSA and laser irradiation demonstrated significant cell death (64.38%), consistent with CCK8 and confocal results. Those *in vitro* PTT experimental results suggested that the PFP@ PPy@BSA nanohybrid could produce a considerable killing effect on A549 cells under laser irradiation.

***In Vivo* Light-Responsive US/PA/^{19}F MR Trimodal Imaging.** In order to test the trimodal imaging ability of PFP@PPy@BSA *in vivo*, US, PA, and MR imaging were performed in subcutaneous A549 tumor-bearing mice via the *i.v.* injection method. The *in vivo* US imaging suggested that
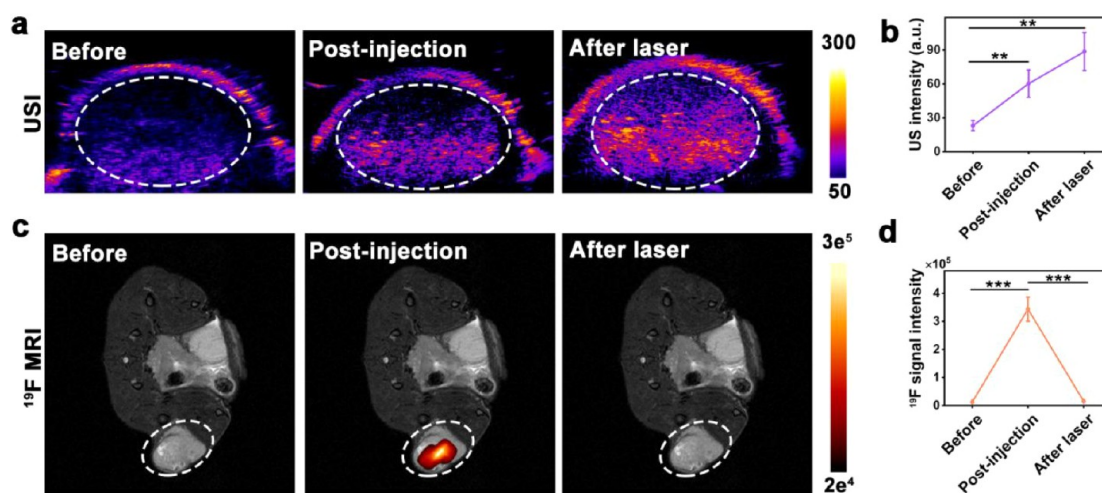
Figure 6. Light-responsive US/^{19}F MR bimodality imaging *in vivo*. (a) US images of subcutaneous A549-tumor-bearing mice and (b) the corresponding US intensity of tumor tissues before injection, 24 h postinjection of PFP@PPy@BSA, and after laser irradiation (1 W/cm^2, 5 min). (c) ^{19}F MRI of subcutaneous A549-tumor-bearing mice and (d) the corresponding ^{19}F MRI signal intensity of tumor tissues before injection, after intratumoral injection of PFP@PPy@BSA (C$_{PFP}$ = 30 mM, 50 μL), and after laser irradiation (0.4 W/cm^2, 30 min). **P < 0.01, and ***P < 0.001, n = 3, data represent mean ± SD.
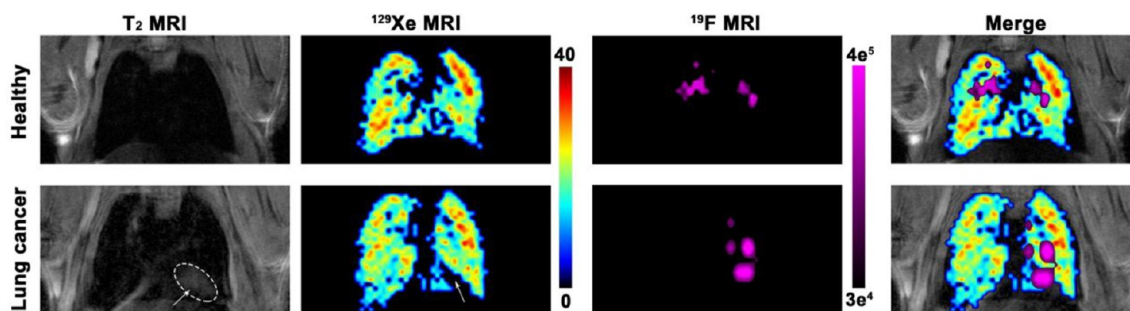

Figure 7. *In vivo* T$_2$ and ^{129}Xe MRI of healthy and orthotopic lung cancer mice, and the ^{19}F MRI of orthotopic lung cancer mice after intratracheally delivered PFP@PPy@BSA (C$_{PFP}$ = 50 mM, 20 μL).

the nanohybrid achieved the highest tumor accumulation at 24 h (C$_{PFP}$ = 18 mM, 200 μL) (Figure 5a and b), indicating that PFP@PPy@BSA could accumulate in the tumor by the EPR effect. Accordingly, after 24 h postinjection, the PA signal achieved the summit, approximately 2-fold higher than preinjection (Figure 5c and d). Beyond that, the strong ^{19}F MRI signal of the tumor was also observed after intratumoral injection of PFP@PPy@BSA (C$_{PFP}$ = 30 mM, 50 μL). The signal nearly diminished until 72 h after injection (Figure 5e and f). Therefore, the PFP@PPy@BSA realized practical multimodal imaging of subcutaneous tumors. After consolidating the tumor accumulation and the *in vivo* trimodal imaging capability of PFP@PPy@BSA, *in vivo* light-responsive US/^{19}F MR bimodal imaging was investigated on the subcutaneous A549 tumor-bearing mice model. Under an 808 nm laser irradiation, the tumor temperature was up to 46 °C, with microbubbles generated. As a result, the echo signal was substantially higher (Figure 6a), reflected in the semiquantification of the US signal (Figure 6b). As expected, the apparent ^{19}F MRI signal of the tumor was weakened upon NIR laser irradiation for 30 min (Figure 6c and d).

To further evaluate the imaging properties of the PFP@PPy@BSA nanohybrid, orthotopic non-small-cell lung cancer (NSCLC) tumors were established using luciferase-labeled A549 cells (A549-Luc). *In vivo* bioluminescence and CT imaging were used to colocate orthotopic lung cancer (Figure S15). Furthermore, T$_2$ and ^{129}Xe MRI jointly confirmed the existence of orthotopic lung cancer. Spectacular imaging effects were obtained against established orthotopic NSCLC tumors after intratracheally delivered PFP@PPy@BSA nanohybrid. ^{19}F MRI showed that the nanohybrid was more inclined to the left lung of nude mice with orthotopic lung cancer, and an obvious ^{19}F MRI signal was observed in the area of orthotopic lung cancer (Figure 7). The above results illustrated that the PFP@PPy@BSA nanohybrid possessed great multimodal imaging potential for subcutaneous tumors and orthotopic lung tumors *in vivo*.

***In Vivo* PTT Therapeutic Effect Evaluation.** Since the final goal of multimodality imaging guidance is for tumor therapy, the therapeutic efficacy of PFP@PPy@BSA for cancer treatment was then studied *in vivo* (Figure 8a). Once the tumor size reached about 80 mm^3, PTT was performed on A549 tumor-bearing mice 24 h postinjection of PFP@PPy@BSA (C$_{PFP}$ = 18 mM, 200 μL). The mice were randomly divided into four groups (four per group) for comparison treatments. Tumor volumes of different treatments were recorded over 20 days to assess the effect of PTT treatment *in vivo*. According to the observations from *in vivo* US and PA images (Figure 5a−d), the maximum tumor enrichment of the probe at 24 h postinjection was selected for PTT. Upon
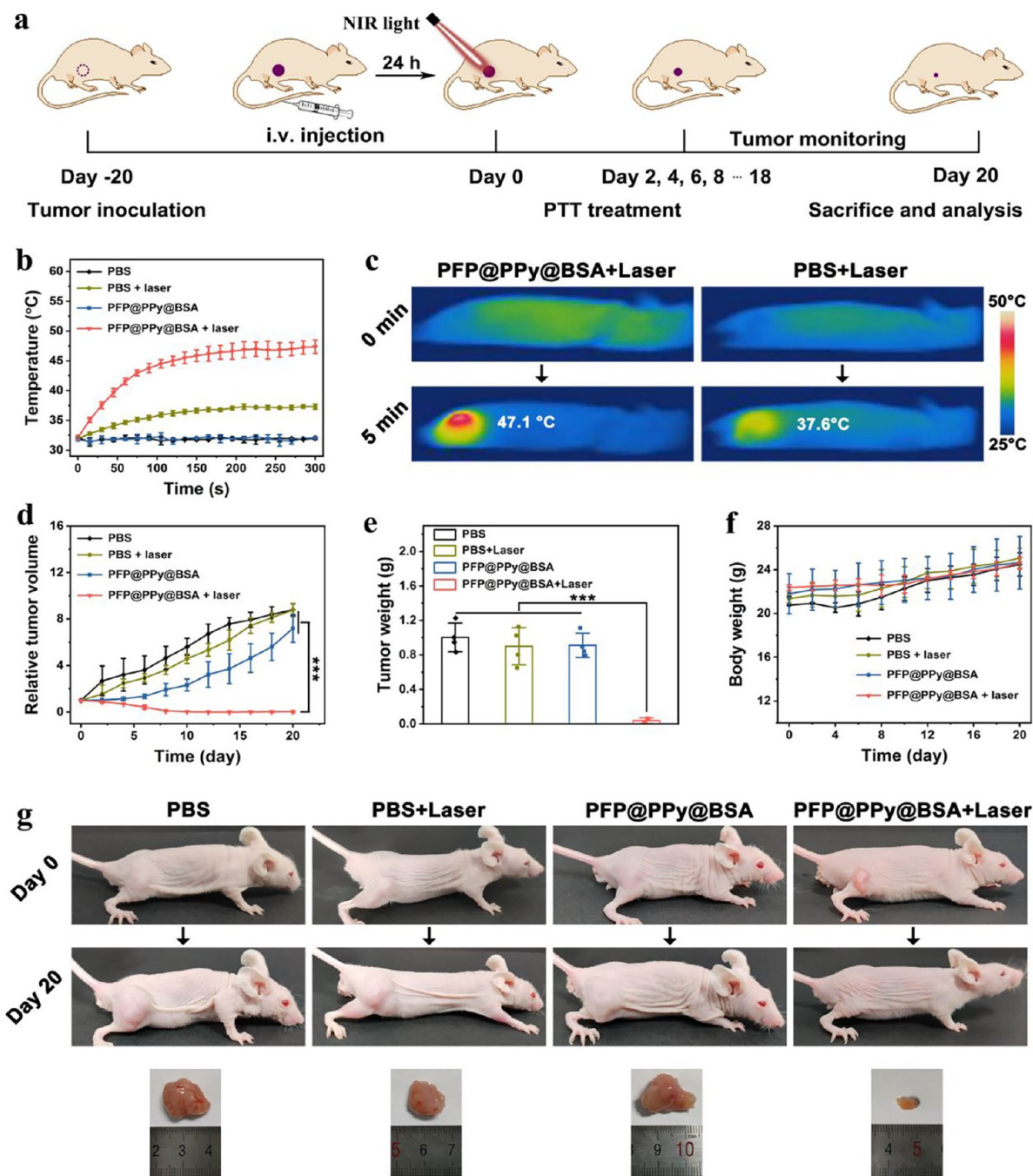
Figure 8. *In vivo* lung cancer phototherapy. (a) Schematic illustration of the treatment procedure for *in vivo* antitumor investigations of nude Balb/c mice bearing A549 tumor. (b) Tumor site temperature elevation of A549 tumors after intravenous injection of PBS or PFP@PPy@BSA under laser irradiation (1 W/cm²). (c) Representative thermal infrared images of mice at 24 h postinjection of PBS or nanohybrid under 5 min of laser irradiation. (d) Tumor volume of four groups after different treatments. (e) Average tumor weight after 20 d of treatment. (f) Mice weight of four groups after different treatments. (g) Photographs of A549 tumor-bearing mice 0 and 20 d after various treatments. ***P < 0.001, n = 4, data represent mean ± SD.

localized 808 nm laser irradiation (1 W/cm²), the temperature changes in the tumor region of tumor-bearing mice were monitored using a thermal infrared camera. The temperature of the tumor tissue in the PFP@PPy@BSA plus laser group increased significantly, reaching about 47.1 °C.

On the contrary, the temperature of the PBS plus laser group improved only slightly (Figure 8b and c). The therapeutic efficacy of PFP@PPy@BSA was assessed by monitoring changes in the tumor volume every two other days, the final

size, and the weight of tumor dissections 20 days after treatments. The results showed that tumors in the PBS, PBS plus laser, and PFP@PPy@BSA groups kept growing similarly. In contrast, the PFP@PPy@BSA plus laser group inhibited tumor growth (Figure 8d), which was attributed to the photothermal effect of PPy. Moreover, the comparison of tumor weight after 20 days of treatment revealed that PFP@PPy@BSA plus laser showed the best result in inhibiting tumor growth with no impact on body weight (Figure 8e and f),

indicating that the designed PTT strategy was feasible. In addition, it could be affirmed in representative pictures of different groups of mice on day 0 and day 20 after treatment (Figure 8g).

To further study the PTT effect of PFP@PPy@BSA on tumor cells, treated tumors were harvested for histological analysis (Figure S16). The H&E staining images of tumors treated with PFP@PPy@BSA plus laser irradiation displayed characteristic apoptosis findings, such as noticeable nucleus shrinkage and cytoplasm leakage. In contrast, the sections of other groups present the densest tumor cells without apparent damage. Correspondingly, prominent apoptosis and reduced proliferative activity were visualized in the PFP@PPy@BSA with laser irradiation group by TUNEL staining and Ki-67 immunohistochemistry assay. These results confirmed that PFP@PPy@BSA mediated PTT inhibited tumor growth via inhibiting proliferation and inducing apoptosis.

Considering the biocompatibility requirement for *in vivo* application, a hemolysis assay was carried out to assess the *in vitro* blood contact safety of the PFP@PPy@BSA nanohybrid. The results showed that the hemolysis rate of the nanohybrid was less than 5%, demonstrating its satisfying biocompatibility for biomedical applications (Figure S17). After 20 days of treatment, each group's main organs and blood were collected for study. There was no prominent inflammation or lesion of the organs between all the groups, confirming ignorable *in vivo* toxicity of the PFP@PPy@BSA in our tested doses (Figure S18a). Moreover, there were no notable differences in blood indexes among the four groups (Figure S18b−m). In brief, the PFP@PPy@BSA nanohybrid can be safely applied to lung cancer diagnosis and PTT.

■ CONCLUSIONS

To summarize, a peculiar photoresponsive theranostic agent on account of the PFP@PPy@BSA nanohybrid was successfully synthesized for highly efficient US/PA/MR trimodal-imaging-guided PTT. *In vitro* and *in vivo* investigations affirmed the nanohybrid's excellent trimodal imaging ability. *In vivo* US/PA imaging exhibited high tumor uptake of the PFP@PPy@BSA nanohybrid after intravenous administration. The as-prepared PFP@PPy@BSA nanohybrid can respond exclusively to the NIR laser. This could lead to the phase transformation of PFP, which significantly enhances the US signal because of the violent release of PFP bubbles and turns the ^{19}F and ^{129}Xe Hyper-CEST MRI signals from "on" to "off". This represents a rare example of an MRI biosensor for biomedical detection based on laser stimulation, which provides a new avenue for developing ^{19}F and ^{129}Xe Hyper-CEST MRI contrast agents. Afterward, mild localized NIR laser irradiation treatment finally resulted in complete inhibition of tumor growth. The PFP@PPy@BSA nanohybrid also owns excellent biocompatibility to promote its application in early diagnosis and PTT of lung cancer or other tumors.

■ EXPERIMENTAL SECTION

Preparation of the PFC@PPy@BSA Nanohybrid. The synthetic route is outlined in Scheme S1. First, 200 μL of PFCs (PFP, PFH, PFOB, PFCE, and PFN) was added into a 5 wt % PVA aqueous solution (5 mL), respectively. The PFC emulsion was generated by pulsed sonication (2 s on, 2 s off) for 40 min. The synthesized emulsion and 1 mL of 0.8 M FeCl$_3$·6H$_2$O were added to water (15 mL) under the stirring

condition of 4 °C. After 30 min, pyrrole (28 μL) was added to the mixture and stirred for 24 h. After that, 200 mg of bovine serum albumin was added to the solution. After stirring for 12 h, the resulting suspension was purified by centrifugation at 2000 rpm for 10 min and was washed several times with water. The gained PFC@PPy@BSA nanohybrid was redispersed in water or PBS buffer for further use.

In Vitro ^{19}F **MRI of Phantoms and Cells.** The ^{19}F MRI experiments were performed on a 9.4 T microimaging system (Bruker, Germany). *In vitro* ^{19}F MR images of PFC@PPy@BSA aqueous solution were acquired through the RARE method (TR = 4000 ms, TE = 3 ms, FOV = 3.7 cm × 3.7 cm, 25 mm slice thickness, RARE factor = 4, matrix size = 32 × 32, 128 averages). For the ^{19}F MRI of cells, both cells were cultured with PFP@PPy@BSA (C$_{PFP}$ = 6 mM) for 12 h at 25 °C and carefully washed with PBS to eliminate the unabsorbed nanohybrid. Subsequently, the cells were scraped from culture flask surfaces with sterile cell scrapers to obtain cell suspensions with a density of approximately 1.8 × 10^7 cells/mL. Afterward, the suspensions were centrifuged to remove the excess PFP@PPy@BSA and prevent the destruction of cell pellets. Then the resuspended cells were used to perform ^{19}F MRI directly using the following parameters: FOV = 3.31 cm × 2.33 cm, 18.5 mm slice thickness, TR = 4000 ms, TE = 3 ms, RARE factor = 4, matrix size = 32 × 32, 128 averages.

In Vitro ^{129}Xe **Hyper-CEST NMR and MRI of Phantoms and Cells.** ^{129}Xe NMR and MRI experiments were conducted on a 400 MHz (9.4 T) Bruker AV400 wide-bore spectrometer, equipped with microimaging gradient coils using home-built continuous-flow equipment to manufacture hyperpolarized ^{129}Xe gas by the spin-exchange optical pumping method. The RF pulse frequency for ^{129}Xe was 110.7 MHz. A gas mixture of 10% N$_2$, 88% He, and 2% Xe flowed through the hyperpolarizer. The gas was bubbled into a 10 mm NMR tube for 20 s, and the spectrum was acquired. The sample temperature was set to 283 K, controlled by the VT unit. Approximately 20% of ^{129}Xe spin polarization was obtained, and NMR spectra for direct detection were processed using a 10 Hz line broadening filter. ^{129}Xe NMR spectra or MRI were acquired using a 10 mm double resonant probe (^{1}H and ^{129}Xe, PA BBO 400 W1/S2 BB-H-D-10Z) with a rectangle flip angle pulse (90°).

For the Hyper-CEST NMR experiments, the samples or cells were added into a 10 mm NMR tube and bubbled using ^{129}Xe gas for 20 s following a delay of 3 s to ensure the bubbles collapsed before signal acquisition. Subsequently, a continuous-wave (CW) saturation pulse with different powers (2, 4, 6, or 8 μT) was swept across 60−220 ppm. The parameters of the MRI experiments were consistent with the NMR scans.

For the ^{129}Xe Hyper-CEST MRI, both the cells were incubated with PFP@PPy@BSA (6 mM) for 12 h at 25 °C, followed by washing with PBS at room temperature and resuspended (5 × 10^6/mL) in 2 mL of PBS for the Hyper CEST experiment (saturation: 5 s, 6.5 μT). The MR images were acquired using a RARE sequence (FOV = 3 cm × 3 cm, matrix size = 32 × 32, slice thickness = 25 mm, echo time = 4.6 ms, repetition time = 5039.7 ms, RARE factor = 8). The ^{129}Xe MR images were segmented using 0.2 × maximum value as the threshold and interpolated into a 64 × 64 image matrix. The on-resonance and off-resonance frequencies of the pulse were set at −121 and 121 ppm, respectively.

In Vitro and ***In Vivo*** **PAI.** All the PAI was performed on a multispectral optoacoustic tomographic system (MOST,

Germany). For the *in vitro* PAI, the sample was put into the mold for determination directly. For the *in vivo* PAI, 200 μL of PFP@PPy@BSA (C_{PFP} = 18 mM) was *i.v.* injected subcutaneously into A549 tumor-bearing mice and imaged at different times.

***In Vitro* and *In Vivo* USI.** All the USI was accomplished by a Vevo 2100 LAZR system. The US imaging and gray values of PFP@PPy@BSA aqueous solutions were obtained with or without laser irradiation. For the *in vivo* US imaging, the nanohybrid (C_{PFP} = 18 mM, 200 μL) was *i.v.* injected subcutaneously into A549 tumor-bearing mice and imaged at different times. Besides, the imaging of the tumor after laser irradiation was performed at the time point of 24 h postinjection.

***In Vivo* ^{19}F MRI.** For the subcutaneous tumor model, the mice were intratumorally injected with 50 μL of PFP@PPy@BSA (C_{PFP} = 30 mM). After a ^{1}H MRI scan using a RARE sequence (TR = 2500 ms, TE = 11 ms, FOV = 3.5 cm × 3.5 cm, 1 mm slice thickness, RARE factor = 8, matrix size = 256 × 256), the ^{19}F MRI was performed through a RARE sequence (TR = 4000 ms, TE = 3 ms, FOV = 4.32 cm × 4.32 cm, 24.7 mm slice thickness, matrix size = 32 × 32, 128 averages). After intratumoral injection and completing a ^{19}F MRI acquisition, the tumors were irradiated with an 808 nm NIR laser (0.4 W/cm^2 for 30 min). The ^{19}F MRI was accomplished at different time points postinjection.

For the orthotopic NSCLC model, the mice were intratracheally delivered of 20 μL of PFP@PPy@BSA (C_{PFP} = 50 mM). After a ^{1}H MRI scan using a RARE sequence (TR = 2500 ms, TE = 11 ms, FOV = 1.88 cm × 2.69 cm, 1 mm slice thickness, RARE factor = 8, matrix size = 256 × 256), the ^{19}F MRI was carried out on a RARE sequence (TR = 4000 ms, TE = 3 ms, FOV = 2.32 cm × 3.32 cm, 24.7 mm slice thickness, matrix size = 32 × 32, 128 averages). All the ^{19}F MR images were segmented using 0.2 × maximum value as the threshold and interpolated into a 128 × 128 matrix.

***In Vivo* Antitumor Effect.** A549 tumor bearing nude mice were assigned into four groups (n = 4 per group) with treatment of (1) PBS; (2) PBS + laser; (3) PFP@PPy@BSA; or (4) PFP@PPy@BSA + laser. The mice received a single dose (200 μL) of intravenous injection, and the administration concentration of PFP@PPy@BSA was 18 mM (C_{PFP}). Twenty-four hours later, the tumors received 808 nm NIR laser irradiation twice for 5 min, with an interval of 5 min. The tumor volume and body weight were monitored every 2 days. The tumor volume was calculated using the following formula: volume (mm^3) = length × width^2/2. Relative tumor volume was defined as V_n/V_0, where V_n and V_0 are the tumor volume measured at Day n and Day 0, respectively.

■ ASSOCIATED CONTENT

ⓢ Supporting Information

The Supporting Information is available free of charge at https://pubs.acs.org/doi/10.1021/acs.bioconjchem.2c00343.

> Experimental materials, instrumentation, and procedures, ^{19}F NMR/MRI, ^{129}Xe NMR, ^{129}Xe Hyper-CEST NMR/MRI, cell cytotoxicity, hemolysis assay, histological examination, and blood indexes data, the relaxation times of PFC@PPy@BSA, and bioluminescence and CT imaging of orthotopic lung cancer (PDF)

■ AUTHOR INFORMATION

Corresponding Author

> **Xin Zhou** − *Key Laboratory of Magnetic Resonance in Biological Systems, State Key Laboratory of Magnetic Resonance and Atomic and Molecular Physics, National Center for Magnetic Resonance in Wuhan, Wuhan Institute of Physics and Mathematics, Innovation Academy for Precision Measurement Science and Technology, Chinese Academy of Sciences-Wuhan National Laboratory for Optoelectronics, Wuhan 430071, P. R. China; University of Chinese Academy of Sciences, Beijing 100049, P. R. China; Optics Valley Laboratory, Hubei 430074, P.R. China;* ⓘ orcid.org/0000-0002-5580-7907; Email: xinzhou@wipm.ac.cn

Authors

> **Shizhen Chen** − *Key Laboratory of Magnetic Resonance in Biological Systems, State Key Laboratory of Magnetic Resonance and Atomic and Molecular Physics, National Center for Magnetic Resonance in Wuhan, Wuhan Institute of Physics and Mathematics, Innovation Academy for Precision Measurement Science and Technology, Chinese Academy of Sciences-Wuhan National Laboratory for Optoelectronics, Wuhan 430071, P. R. China; University of Chinese Academy of Sciences, Beijing 100049, P. R. China; Optics Valley Laboratory, Hubei 430074, P.R. China*

> **Maosong Qiu** − *Key Laboratory of Magnetic Resonance in Biological Systems, State Key Laboratory of Magnetic Resonance and Atomic and Molecular Physics, National Center for Magnetic Resonance in Wuhan, Wuhan Institute of Physics and Mathematics, Innovation Academy for Precision Measurement Science and Technology, Chinese Academy of Sciences-Wuhan National Laboratory for Optoelectronics, Wuhan 430071, P. R. China; University of Chinese Academy of Sciences, Beijing 100049, P. R. China*

> **Ruifang Wang** − *Key Laboratory of Magnetic Resonance in Biological Systems, State Key Laboratory of Magnetic Resonance and Atomic and Molecular Physics, National Center for Magnetic Resonance in Wuhan, Wuhan Institute of Physics and Mathematics, Innovation Academy for Precision Measurement Science and Technology, Chinese Academy of Sciences-Wuhan National Laboratory for Optoelectronics, Wuhan 430071, P. R. China; University of Chinese Academy of Sciences, Beijing 100049, P. R. China*

> **Lei Zhang** − *Key Laboratory of Magnetic Resonance in Biological Systems, State Key Laboratory of Magnetic Resonance and Atomic and Molecular Physics, National Center for Magnetic Resonance in Wuhan, Wuhan Institute of Physics and Mathematics, Innovation Academy for Precision Measurement Science and Technology, Chinese Academy of Sciences-Wuhan National Laboratory for Optoelectronics, Wuhan 430071, P. R. China; University of Chinese Academy of Sciences, Beijing 100049, P. R. China; Optics Valley Laboratory, Hubei 430074, P.R. China*

> **Conggang Li** − *Key Laboratory of Magnetic Resonance in Biological Systems, State Key Laboratory of Magnetic Resonance and Atomic and Molecular Physics, National Center for Magnetic Resonance in Wuhan, Wuhan Institute of Physics and Mathematics, Innovation Academy for Precision Measurement Science and Technology, Chinese Academy of Sciences-Wuhan National Laboratory for Optoelectronics, Wuhan 430071, P. R. China; University of Chinese Academy of Sciences, Beijing 100049, P. R. China; Optics Valley*

Laboratory, Hubei 430074, P.R. China; ⊙ orcid.org/0000-0002-5798-1722

Chaohui Ye − *Key Laboratory of Magnetic Resonance in Biological Systems, State Key Laboratory of Magnetic Resonance and Atomic and Molecular Physics, National Center for Magnetic Resonance in Wuhan, Wuhan Institute of Physics and Mathematics, Innovation Academy for Precision Measurement Science and Technology, Chinese Academy of Sciences-Wuhan National Laboratory for Optoelectronics, Wuhan 430071, P. R. China; University of Chinese Academy of Sciences, Beijing 100049, P. R. China; Optics Valley Laboratory, Hubei 430074, P.R. China*

Complete contact information is available at:
https://pubs.acs.org/10.1021/acs.bioconjchem.2c00343

Author Contributions

Notes

■ ACKNOWLEDGMENTS

■ REFERENCES

(1) Oudkerk, M.; Liu, S.; Heuvelmans, M. A.; Walter, J. E.; Field, J. K. *Nat. Rev. Clin. Oncol.* **2021**, *18*, 135−151.

(2) Bracken-Clarke, D.; Kapoor, D.; Baird, A. M.; Buchanan, P. J.; Finn, S. P. Vaping and lung cancer − A review of current data and recommendations. *Lung Cancer* **2021**, *153*, 11−20.

(3) Liu, Y.; Li, Y.; Koo, S.; Sun, Y.; Liu, Y.; Liu, X.; Pan, Y.; Zhang, Z.; Du, M.; Lu, S.; et al. *Chem. Rev.* **2022**, *122*, 209−268.

(4) Song, J.; Huang, P.; Duan, H.; Chen, X. *Acc. Chem. Res.* **2015**, *48*, 2506−2515.

(5) Wang, J.; Tao, W.; Chen, X.; Farokhzad, O. C.; Liu, G. *Theranostics* **2017**, *7*, 3915−3919.

(6) Gao, P.; Chen, Y.; Pan, W.; Li, N.; Liu, Z.; Tang, B. *Angew. Chem., Int. Ed.* **2021**, *60*, 16763−16776.

(7) Jin, Q.; Zhu, W.; Zhu, J.; Zhu, J.; Shen, J.; Liu, Z.; Yang, Y.; Chen, Q. Nanoparticle-Mediated Delivery of Inhaled Immunotherapeutics for Treating Lung Metastasis. *Adv. Mater.* **2021**, *33*, e2007557.

(8) Sun, L.; Shen, F.; Xiong, Z.; Yang, H.; Dong, Z.; Xiang, J.; Gu, Q.; Ji, Q.; Fan, C.; Liu, Z. *J. Am. Chem. Soc.* **2022**, *144*, 7634−7645.

(9) Ding, F.; Feng, J.; Zhang, X.; Sun, J.; Fan, C.; Ge, Z. *Adv. Drug. Delivery Rev.* **2021**, *173*, 141−163.

(10) Zhu, B.; Wang, L.; Li, J.; Fan, C. *Chem. Rec.* **2017**, *17*, 1213−1230.

(11) Fan, Q.; Cheng, K.; Hu, X.; Ma, X.; Zhang, R.; Yang, M.; Lu, X.; Xing, L.; Huang, W.; Gambhir, S. S. Transferring Biomarker into Molecular Probe: Melanin Nanoparticle as a Naturally Active

Platform for Multimodality Imaging. *J. Am. Chem. Soc.* **2014**, *136*, 15185−15194.

(12) Liu, H.; Lin, W.; He, L.; Chen, T. *Biomaterials* **2020**, *226*, 119545−119557.

(13) Wang, J.; Liu, J.; Liu, Y.; Wang, L.; Zhao, Y. Gd-Hybridized Plasmonic Au-Nanocomposites Enhanced Tumor-Interior Drug Permeability in Multimodal Imaging-Guided Therapy. *Adv. Mater.* **2016**, *28*, 8950−8958.

(14) Yang, Y.; Wu, H.; Liu, B.; Liu, Z. *Adv. Drug. Delivery Rev.* **2021**, *179*, 114004.

(15) Wang, X.; Zhong, X.; Li, J.; Liu, Z.; Cheng, L. *Chem. Soc. Rev.* **2021**, *50*, 8669−8742.

(16) Song, W.; Song, Y.; Li, Q.; Fan, C.; Lan, X.; Jiang, D. *Eur. J. Nucl. Med. Mol. Imaging* **2022**, *49*, 2544−2559.

(17) Xie, X.; Hu, X.; Li, Q.; Yin, M.; Song, H.; Hu, J.; Wang, L.; Fan, C.; Chen, N. *Nano Lett.* **2020**, *20*, 5228−5235.

(18) Lin, J.; Wang, M.; Hu, H.; Yang, X.; Wen, B.; Wang, Z.; Jacobson, O.; Song, J.; Zhang, G.; Niu, G.; et al. *Adv. Mater.* **2016**, *28*, 3273−3279.

(19) Wang, M.; Yang, Q.; Li, M.; Zou, H.; Wang, Z.; Ran, H.; Zheng, Y.; Jian, J.; Zhou, Y.; Luo, Y.; et al. *ACS Appl. Mater. Interfaces* **2020**, *12*, 5642−5657.

(20) Chen, X.; Zhang, Y.; Zhang, H.; Zhang, L.; Liu, L.; Cao, Y.; Ran, H.; Tian, J. A non-invasive nanoparticles for multimodal imaging of ischemic myocardium in rats. *J. Nanobiotechnol.* **2021**, *19*, 82−99.

(21) Liu, S.; Zhang, W.; Chen, Q.; Hou, J.; Wang, J.; Zhong, Y.; Wang, X.; Jiang, W.; Ran, H.; Guo, D. *Nanoscale* **2021**, *13*, 14049−14066.

(22) Park, S.; Jang, J.; Kim, J.; Kim, Y. S.; Kim, C. *IEEE Trans. Med. Imaging* **2017**, *36*, 1912−1921.

(23) Ehlerding, E. B.; Grodzinski, P.; Cai, W.; Liu, C. H. *ACS Nano* **2018**, *12*, 2106−2121.

(24) Siwawannapong, K.; Zhang, R.; Lei, H.; Jin, Q.; Tang, W.; Dong, Z.; Lai, R. Y.; Liu, Z.; Kamkaew, A.; Cheng, L. *Theranostics* **2020**, *10*, 62−73.

(25) Kong, H.; Zhang, J.; Li, J.; Wang, J.; Shin, H. J.; Tai, R.; Yan, Q.; Xia, K.; Hu, J.; Wang, L.; et al. *Natl. Sci. Rev.* **2020**, *7*, 1218−1227.

(26) Düwel, S.; Hundshammer, C.; Gersch, M.; Feuerecker, B.; Steiger, K.; Buck, A.; Walch, A.; Haase, A.; Glaser, S. J.; Schwaiger, M. Imaging of pH in vivo using hyperpolarized 13C-labelled zymonic acid. *Nat. Commun.* **2017**, *8*, 15126−15134.

(27) Wei, H.; Wisniowska, A.; Fan, J.; Harvey, P.; Li, Y.; Wu, V.; Hansen, E. C.; Zhang, J.; Kaul, M. G.; Frey, A. M; Adam, G.; Frenkel, A. I.; Bawendi, M. G.; Jasanoff, A. Single-nanometer iron oxide nanoparticles as tissue-permeable MRI contrast agents. *Proc. Natl. Acad. Sci. U. S. A.* **2021**, *118*, e2102340118.

(28) Cai, X.; Zhu, Q.; Zeng, Y.; Zeng, Q.; Zhan, Y. Manganese Oxide Nanoparticles As MRI Contrast Agents In Tumor Multimodal Imaging And Therapy. *Int. J. Nanomed.* **2019**, *14*, 8321−8344.

(29) Jiang, G.; Fan, D.; Tian, J.; Xiang, Z.; Fang, Q. Self-Confirming Magnetosomes for Tumor-Targeted T1/T2 Dual-Mode MRI and MRI-Guided Photothermal Therapy. *Adv. Healthc. Mater.* **2022**, *11*, e2200841.

(30) Ren, J.; Tang, X.; Wang, T.; Wei, X.; Zhang, J.; Lu, L.; Liu, Y.; Yang, B. A Dual-Modal Magnetic Resonance/Photoacoustic Imaging Tracer for Long-Term High-Precision Tracking and Facilitating Repair of Peripheral Nerve Injuries. *Adv. Healthc. Mater.* **2022**, *11*, e2200183.

(31) Khan, A. S.; Harvey, R. L.; Birchall, J. R.; Irwin, R. K.; Nikolaou, P.; Schrank, G.; Emami, K.; Dummer, A.; Barlow, M. J.; Goodson, B. M.; et al. *Angew. Chem., Int. Ed.* **2021**, *60*, 22126−22147.

(32) Janasik, D.; Krawczyk, T. 19F MRI Probes for Multimodal Imaging. *Chemistry - A European Journal* **2022**, *28*, e202102556.

(33) Deng, H.; Duan, C.; Xiao, S.; Xie, J.; Zhang, H.; Sun, X.; Zhou, X. *IEEE Trans. Instrum. Meas.* **2019**, *68*, 3950−3961.

(34) Tirotta, I.; Dichiarante, V.; Pigliacelli, C.; Cavallo, G.; Terraneo, G.; Bombelli, F. B.; Metrangolo, P.; Resnati, G. 19F Magnetic Resonance Imaging (MRI): From Design of Materials to Clinical Applications. *Chem. Rev.* **2015**, *115*, 1106−1129.

(35) Zhang, H.; Chen, S.; Yuan, Y.; Li, Y.; Jiang, Z.; Zhou, X. *ACS Appl. Bio Mater.* **2019**, *2*, 27−32.

(36) Li, S.; Jiang, W.; Yuan, Y.; Sui, M.; Yang, Y.; Huang, L.; Jiang, L.; Liu, M.; Chen, S.; Zhou, X. *ACS Appl. Mater. Interfaces* **2020**, *12*, 57290−57301.

(37) Yang, Y.; Zhang, Y.; Wang, B.; Guo, Q.; Yuan, Y.; Jiang, W.; Shi, L.; Yang, M.; Chen, S.; Lou, X.; et al. *Chem. Sci.* **2021**, *12*, 4300−4308.

(38) Zeng, Q.; Bie, B.; Guo, Q.; Yuan, Y.; Han, Q.; Han, X.; Chen, M.; Zhang, X.; Yang, Y.; Liu, M.; et al. *Proc. Natl. Acad. Sci. U. S. A.* **2020**, *117*, 17558−17563.

(39) Li, H.; Zhao, X.; Wang, Y.; Lou, X.; Chen, S.; Deng, H.; Shi, L.; Xie, J.; Tang, D.; Zhao, J.; et al. Damaged lung gas exchange function of discharged COVID-19 patients detected by hyperpolarized 129Xe MRI. *Sci. Adv.* **2021**, *7*, eabc8180.

(40) Sun, S.; Song, Y.; Chen, J.; Huo, M.; Chen, Y.; Sun, L. *Nanoscale* **2021**, *13*, 18300−18310.

(41) Yi, X.; Zhou, H.; Chao, Y.; Xiong, S.; Zhong, J.; Chai, Z.; Yang, K.; Liu, Z. Bacteria-triggered tumor-specific thrombosis to enable potent photothermal immunotherapy of cancer. *Sci. Adv.* **2020**, *6*, eaba3546.

(42) Li, X.; Lovell, J. F.; Yoon, J.; Chen, X. *Nat. Rev. Clin. Oncol.* **2020**, *17*, 657−674.

(43) Wang, X.; Ma, Y.; Sheng, X.; Wang, Y.; Xu, H. *Nano Lett.* **2018**, *18*, 2217−2225.

(44) Lu, T. Y.; Chiang, C. Y.; Fan, Y. J.; Jheng, P. R.; Quiñones, E. D.; Liu, K. T.; Kuo, S. H.; Hsieh, H. Y.; Tseng, C. L.; Yu, J.; et al. *ACS Appl. Mater. Interfaces* **2021**, *13*, 10287−10300.

(45) Pu, X. Q.; Ju, X. J.; Zhang, L.; Cai, Q. W.; Liu, Y. Q.; Peng, H. Y.; Xie, R.; Wang, W.; Liu, Z.; Chu, L. Y. *ACS Appl. Mater. Interfaces* **2021**, *13*, 28802−28817.

(46) Chen, Y. S.; Zhao, Y.; Yoon, S. J.; Gambhir, S. S.; Emelianov, S. *Nat. Nanotechnol.* **2019**, *14*, 465−472.

(47) Busquets, M. A.; Estelrich, J. *Drug Discovery Today* **2020**, *25*, 1431−1443.

(48) Zhang, C.; Sun, W.; Wang, Y.; Xu, F.; Shi, X. Gd-/CuS-Loaded Functional Nanogels for MR/PA Imaging-Guided Tumor-Targeted Photothermal Therapy. *ACS Appl. Mater. Interfaces* **2020**, *12*, 9107−9117.

(49) Feng, W.; Han, X.; Wang, R.; Gao, X.; Hu, P.; Yue, W.; Chen, Y.; Shi, J. Nanocatalysts-Augmented and Photothermal-Enhanced Tumor-Specific Sequential Nanocatalytic Therapy in Both NIR-I and NIR-II Biowindows. *Adv. Mater.* **2019**, *31*, 1805919−1805932.

(50) Zhou, B.; Yin, C.; Feng, Q.; Wu, Y.; Pan, X.; Liu, C.; Tian, J.; Geng, S.; Wang, K.; Xing, J.; et al. *Nanoscale* **2021**, *13*, 19085−19097.

(51) Yan, R.; Hu, Y.; Liu, F.; Wei, S.; Fang, D.; Shuhendler, A. J.; Liu, H.; Chen, H. Y.; Ye, D. *J. Am. Chem. Soc.* **2019**, *141*, 10331−10341.

(52) He, T.; Qin, X. L.; Jiang, C.; Jiang, D. W.; Lei, S.; Lin, J.; Zhu, W. G.; Qu, J. L.; Huang, P. *Theranostics* **2020**, *10*, 2453−2462.

(53) Li, Z. L.; Hu, Y.; Miao, Z. H.; Xu, H.; Li, C. X.; Zhao, Y.; Li, Z.; Chang, M. L.; Ma, Z.; Sun, Y.; et al. *Nano Lett.* **2018**, *18*, 6778−6788.

(54) Chen, L.; Zhou, X. J.; Nie, W.; Feng, W.; Zhang, Q. Q.; Wang, W. Z.; Zhang, Y. Z.; Chen, Z. G.; Huang, P.; He, C. L. *ACS Appl. Mater. Interfaces* **2017**, *9*, 17786−17798.

(55) Tao, W.; Ji, X.; Xu, X.; Ariful Islam, M.; Li, Z.; Chen, S.; Saw, P. E.; Zhang, H.; Bharwani, Z.; Guo, Z.; et al. Antimonene Quantum Dots: Synthesis and Application as Near-Infrared Photothermal Agents for Effective Cancer Therapy. *Angew. Chem., Int. Ed.* **2017**, *56*, 11896−11900.

(56) Yang, Q.; Chen, H.; Bai, Y.; Cao, Y.; Hu, W.; Zhang, L. *Adv. Healthc. Mater.* **2018**, *7*, 1700816−1700825.

(57) Ektate, K.; Kapoor, A.; Maples, D.; Tuysuzoglu, A.; Vanosdol, J.; Ramasami, S.; Ranjan, A. *Theranostics* **2016**, *6*, 1963−1974.

📖 **Recommended by ACS**

Two-Stage Targeted Bismuthene-Based Composite Nanosystem for Multimodal Imaging Guided Enhanced Hyperthermia and Inhibition of Tumor Recurrence

Lei Bai, Jin Hou, *et al.*

MAY 24, 2022
ACS APPLIED MATERIALS & INTERFACES   READ 🔗

Hollow Manganese-Doped Calcium Phosphate Nanoparticles Treated with Melanin Nanoparticles and Thalidomide for Photothermal and Anti-angiogenic Cancer Therapy

Juan Li, Ruiping Zhang, *et al.*

MAY 27, 2022
ACS APPLIED NANO MATERIALS   READ 🔗

Near-Infrared Responsive Synergistic Chemo-Phototherapy from Surface-Functionalized Poly(ε-caprolactone)–Poly(d,l-lactic-*co*-glycolic acid) Composite Nanofibers for Postsurg...

Jakia Khanom, Cheol Sang Kim, *et al.*

AUGUST 10, 2022
BIOMACROMOLECULES   READ 🔗

Effect of Doxorubicin on the Near-Infrared Optical Properties of Indocyanine Green

Saumya Jaiswal, Sharad Gupta, *et al.*

DECEMBER 10, 2021
ACS OMEGA   READ 🔗

Get More Suggestions >